Review

Topological kagome magnets and superconductors

https://doi.org/10.1038/s41586-022-05516-0

Received: 4 June 2022

Accepted: 2 November 2022

Published online: 21 December 2022

Check for updates

Jia-Xin Yin[1,2] ✉, Biao Lian[1] ✉ & M. Zahid Hasan[1,3,4,5] ✉

A kagome lattice naturally features Dirac fermions, flat bands and van Hove singularities in its electronic structure. The Dirac fermions encode topology, flat bands favour correlated phenomena such as magnetism, and van Hove singularities can lead to instabilities towards long-range many-body orders, altogether allowing for the realization and discovery of a series of topological kagome magnets and superconductors with exotic properties. Recent progress in exploring kagome materials has revealed rich emergent phenomena resulting from the quantum interactions between geometry, topology, spin and correlation. Here we review these key developments in this field, starting from the fundamental concepts of a kagome lattice, to the realizations of Chern and Weyl topological magnetism, to various flat-band many-body correlations, and then to the puzzles of unconventional charge-density waves and superconductivity. We highlight the connection between theoretical ideas and experimental observations, and the bond between quantum interactions within kagome magnets and kagome superconductors, as well as their relation to the concepts in topological insulators, topological superconductors, Weyl semimetals and high-temperature superconductors. These developments broadly bridge topological quantum physics and correlated many-body physics in a wide range of bulk materials and substantially advance the frontier of topological quantum matter.

A kagome lattice (Fig. 1a), made of corner-sharing triangles, is a geometrically frustrated two-dimensional (2D) lattice introduced to quantum physics[1] in 1951, as an analogy to a type of bamboo basket used in eastern countries. Interestingly, the kagome pattern has no direct analogy to wild nature, but a similar pattern has long been used as the star of David in religious ceremonies and a hexagram in alchemy symbols. In quantum physics research, inspired by Onsager's exact solution of the Ising model for the square lattice[2] in the 1940s, researchers extended the study of magnetic phase transitions to triangular, honeycomb and, eventually, kagome lattices. In the 1951 kagome work[1], Syôzi demonstrated that, in contrast to the ferromagnetic case, a phase transition does not occur in a kagome lattice with a nearest-neighbour antiferromagnetic Ising interaction. Nowadays, geometrical spin frustration in a kagome lattice under an antiferromagnetic exchange interaction is widely appreciated, and shows a great potential to realize quantum-spin-liquid states[3] that feature long-range quantum entanglement, fractionalized excitations and the absence of ordinary magnetic order[4]. Although these studies are about Heisenberg spins in a kagome lattice, there has long been a debate about quantum magnetism since the 1930s: Heisenberg's view that magnetic moments come from electrons localized in atoms[5], or Stoner's view that magnetization collectively arises from itinerant electrons[6]. Under this broad context, in the 1991 kagome work[7], Mielke studied the Hubbard model of a kagome lattice, and demonstrated that the flat band in its electronic structure stabilizes the ferromagnetic ground state. Finally, through this early quantum magnetism research, the electronic structure of the kagome lattice was unveiled and its power began to emerge[8].

Fundamental concepts for kagome electrons

For a kagome lattice electron tight-binding Hamiltonian $H = -\sum_{\langle ij\rangle, s_z=\pm\frac{1}{2}} (tc^{\dagger}_{i,s_z}c_{j,s_z} + \text{h.c.})$ with a real nearest-neighbour (denoted by $\langle ij\rangle$) hopping $-t$ (where $c^{\dagger}_{i,s_z}$ and c_{i,s_z} are the spin s_z electron creation and annihilation operators, respectively, on site i, and h.c. is the hermitian conjugate), its electronic band structure exhibits an exactly flat band at energy $2t$ in the whole Brillouin zone, in quadratic band touching with the neighbouring band (Fig. 1b). This flat band originates from subdimensional eigen-wavefunctions with exact cancellation of hoppings due to lattice geometry, which can be generalized into a class of tight-binding models called line graphs[7,9]. Moreover, the band structure features Dirac cones at the Brillouin zone corners, and two van Hove singularities at the Brillouin zone boundaries (Fig. 1b,c). Theoretical understanding of the emergent physics of kagome electrons has deepened along with the introduction of theories on topological quantum matter[10–12] and high-temperature-superconductivity-type correlated many-body physics[13] to kagome systems.

A pioneering idea[14] is that, by a hopping flux $\phi = 0$ and $\phi = \pi$ in each triangle plaquette (Fig. 1a), energy gaps can be opened at the Dirac points between the two dispersive bands and the quadratic band touching point between the flat band and its neighbouring band, which leads

[1]Department of Physics, Princeton University, Princeton, NJ, USA. [2]Department of Physics, Southern University of Science and Technology, Shenzhen, China. [3]Princeton Institute for the Science and Technology of Materials, Princeton University, Princeton, NJ, USA. [4]Materials Sciences Division, Lawrence Berkeley National Laboratory, Berkeley, CA, USA. [5]Quantum Science Center, Oak Ridge, TN, USA. ✉e-mail: yinjx@sustech.edu.cn; biao@princeton.edu; mzhasan@princeton.edu

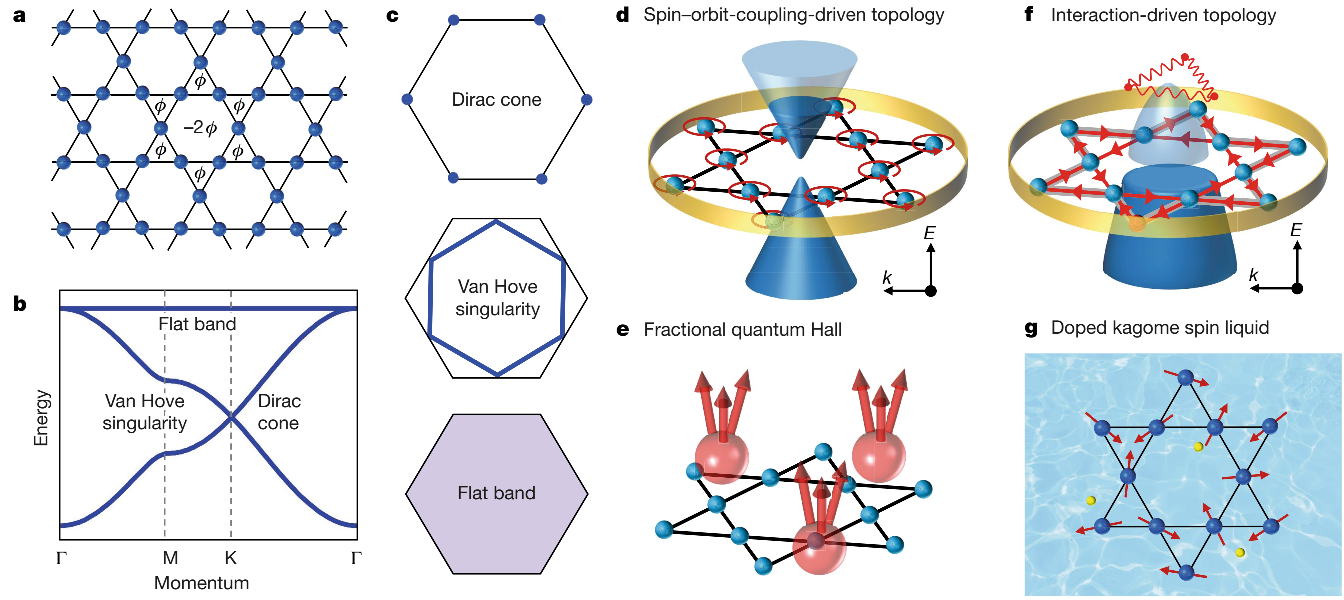

Fig. 1 | Fundamental concepts of kagome electrons. a, A kagome lattice made of corner-sharing triangles. Each triangle can carry a quantum flux ϕ, and each hexagon carries a quantum flux -2ϕ. **b**, Band structure of a kagome lattice considering the nearest-neighbour electron hopping term with $\phi = 0$. This band structure contains three key features: Dirac cones at K (or K′) points, van Hove singularities at M points and a flat band in the momentum space. **c**, Contour of the Fermi surfaces in the momentum space at Dirac cone (top), van Hove singularity (middle) and flat band (bottom) energies, respectively. **d**, Atomic spin–orbit-coupling-driven (red circular arrows) topology in a kagome lattice (blue spheres). The spin–orbit coupling opens a topological gap at the Dirac cone (blue cones) in the band structure (by producing a non-zero ϕ), and induces a topological edge state (yellow ring). The light (dark) blue cone represents unoccupied (occupied) electronic states, illustrating the generic case of Fermi energy away from the Dirac gap. **e**, Illustration of a flat-band-driven fractional Chern insulator in a kagome lattice (blue spheres). The red spheres illustrate electrons bound with an odd number of Berry flux quanta in the ground state. **f**, Many-body-interaction-driven (red wavy lines) topology in the kagome lattice (blue spheres). The interaction (which can be related to van Hove singularities) not only opens a charge gap at the Fermi energy but also produces a non-trivial Berry phase that leads to orbital currents (red arrows) and a topological edge state (yellow ring). The light and dark blue cones represent unoccupied and occupied electronic states, respectively. Compared with the spin–orbit-coupling-driven topology that often opens the topological gap away from the Fermi energy, the interaction-driven topology may open the topological gap directly at the Fermi level through long-range orders even without Dirac fermions. **g**, Doped kagome spin liquid as initially proposed for unconventional superconductivity in the kagome lattice. The blue spheres denote the kagome lattice, the red arrows denote local spins and the yellow spheres denote doped charge carriers.

to a Chern number $C = \pm1, 0, \mp1$ in the three bands (in energetic order), in resemblance to the Haldane model for the honeycomb lattice[15]. Each occupied band then contributes a quantized Hall conductance $\sigma_{xy} = Ce^2/h$ (where e is the elemental charge and h is Planck's constant). The flux ϕ amounts to having a complex hopping $-t - i\lambda' = -|t'|\, e^{i\phi/3}$ anticlockwise in each triangle (where $-\lambda'$ is the imaginary part of the complex hopping $-t'$), which can arise from the spin Berry phase in a kagome magnet with a chiral spin texture[14]. With the conceptual development of the quantum spin Hall effect and Z_2 topological number[16,17], the Kane–Mele type of spin–orbit coupling was also introduced to the kagome lattice[18–20] (Fig. 1d), which takes the form $H_{soc} = -\lambda \sum_{\langle i\to j\rangle, s_z=\pm\frac{1}{2}} 2s_z(ic^\dagger_{i,s_z}c_{j,s_z} + \mathrm{h.c.})$, where $\langle i \to j\rangle$ is nearest-neighbour pointing anticlockwise in a triangle, and λ is the spin–orbit coupling strength. It induces opposite fluxes $\pm\phi$ for opposite spins $s_z = \pm1/2$ and opens spin Chern gaps. The gap opened at either the Dirac points or the flat-band quadratic band touching is Z_2 topologically non-trivial (quantum spin Hall), which will develop helical edge states protected by time-reversal symmetry. By further adding an out-of-plane magnetization $H_{M_z} = -M_z \sum_{i,s_z=\pm\frac{1}{2}} s_z c^\dagger_{i,s_z} c_{i,s_z}$ to the kagome lattice (where M_z is the z-direction Zeeman field) that lifts the spin $s = \pm1/2$ degeneracy, the Z_2 topological gap becomes a Chern gap, and the kagome lattice carries a chiral edge state correspondingly. In kagome lattice materials, magnetism often arises spontaneously, making such a scenario possible. When the Fermi level is filled within the Chern gap, the kagome lattice exhibits a quantized anomalous Hall effect[20]. When the electron filling is away from the Chern gap, the total Berry curvature below the Fermi level will contribute to the anomalous Hall conductivity $\sigma_{xy} \approx \frac{\Delta}{2|E_D|}\frac{e^2}{h}$, where Δ is the Chern gap size (twice the Dirac mass) and E_D is the Dirac Fermi energy measured from the mid-gap energy. When the sizes of Δ and E_D are comparable, the Berry curvature effect is still substantial, leading to a giant or large anomalous Hall effect that is often reported for topological kagome magnets. Moreover, as the Kane–Mele-type spin–orbit coupling H_{soc} is proportional to the out-of-plane spin s_z, a sufficiently large in-plane magnetization $H_{M_x} = -M_x \sum_{i,s_z,s_z'} c^\dagger_{i,s_z}(\sigma_x)_{s_z,s_z'} c_{i,s_z}$ (where M_x is the x-direction Zeeman field) will polarize spins in-plane, making H_{soc} effectively zero and closing the topological gap. This spin–orbit tunability leads to magnetization direction control of the quantum-state topology of the kagome lattice, which is broadly discussed in topological kagome materials with soft magnetism. Similar topological physics induced by spin–orbital coupling and magnetism can also occur when the Fermi level is between the flat band and its neighbouring band. In reality, most kagome materials are three-dimensional (3D) materials consisting of stacked kagome lattice layers, and the above physics of the kagome lattice emerges in each layer in the weak-interlayer-coupling regime. Such layered kagome materials with the Fermi level in the Chern gap exhibit the 3D quantum anomalous Hall effect[21]. When the interlayer coupling is strong, the dispersion can have a strong z-direction (perpendicular to layers) momentum (k_z) dependence. If one views the band structure at each fixed k_z as a 2D kagome system, its Chern gap can also undergo gap closings as a function of k_z, which correspond to Weyl points in the 3D Brillouin zone[22–24].

In parallel to the topological bands, the many-body interactions of kagome electrons is another research frontier for kagome materials.

Since the discovery of copper-based and iron-based high-temperature superconductivity, it has been widely appreciated that many-body correlations lie at the heart of most exotic quantum phases of matter[13]. For kagome electrons, the initial interest is in the realization of a flat band. Benefiting from quenched kinetic energy, flat bands can host correlated electronic states, including ferromagnetism[7], which is often detected in kagome lattice materials. As discussed earlier, the spin–orbit coupling can open a Chern gap at both the Dirac cone and the quadratic band touching point of the flat band in the magnetic kagome lattice. At a partial filling of the flat band, a kagome lattice with interactions has the potential to realize fractionalized topological phases, such as the fractional Chern insulator (fractional quantum Hall states without magnetic field)[19,25–27] (Fig. 1e). Soon after these flat-band concepts were established, substantial interest was focused on the possible electronic orders at the van Hove filling[28–30], where the Fermi surface is nested and has saddle points on the edges of the Brillouin zone. The real-space superlattice for the nesting vector gives a 2 × 2-unit-cell enlarging, and various kinds of spin density wave, charge-density wave and nematicity order with similar wavevectors have been proposed[28–30]. These orders also serve as a precursor of unconventional superconductivity in the kagome lattice and are broadly relevant to kagome superconductors. One intriguing charge order under consideration of the extended Coulomb interaction is one that leads to orbital currents and breaks time-reversal symmetry[30]. A similar orbital-currents scenario has also been proposed for the kagome flat-band full filling that leads to the quantum anomalous Hall effect[31]. More broadly, the orbital-currents physics in a kagome lattice resembles the loop current proposal for cuprates as an attempt to understand the pseudogap physics[32], and effectively realizes the Haldane model phase[15]. Compared with spin–orbit-coupling-driven topology, interaction-driven topology (defined as topology from order induced by many-body interactions of the active band electrons) may open the topological gap directly at the Fermi level (Fig. 1f). In addition, the time-reversal-symmetry-breaking charge order links the kagome magnetism and kagome superconductivity. In fact, the initially proposed kagome superconductivity is through doping a kagome spin liquid[33] (Fig. 1g), where the superconducting order breaks the time-reversal symmetry.

In realizing these concepts, advanced techniques have been applied in probing kagome electrons. Magneto-transport can probe the phase transition and Berry curvature, but it is sensitive to only the electronic states at the Fermi level. Angle-resolved photoemission probes the band dispersions, but it lacks magnetic tunability and integrates different magnetic domains. Scanning tunnelling microscopy can probe the local density of states under a magnetic field, but it is sensitive to only electronic states of the surface kagome layer. Scattering techniques can probe the bulk spin and lattice order, but they often lack charge and orbital sensitivity. First-principles calculations are powerful in identifying the topological index of the electronic structure, but correlations associated with magnetism lead to a non-rigid band shift so the chemical potential and band renormalization require corrections in reference to the experimental data. Therefore, these complementary techniques need to be combined to determine the topological or many-body effects of kagome electrons.

Chern quantum phase and spin–orbit tunability

During studies of topological magnets, several transition-metal-based kagome materials came to researchers' attention, initially owing to their large anomalous Hall effect[34–37]. As learned from the quantum Hall effect, the topological nature of the anomalous Hall effect (that is, the intrinsic Berry curvature contribution) had readily been widely appreciated[38] at the time of these studies in kagome materials, especially after the experimental realization of the quantum anomalous Hall effect[39]. One natural explanation would be to associate the anomalous Hall effect with the Berry curvature near the topological gap in the spin–orbit-coupled kagome bands. In the ferromagnet Fe_3Sn_2, photoemission and tunnelling experiments have detected Dirac-like gaps[40,41] and a kagome bilayer electronic structure has been identified. However, Fe_3Sn_2 is a soft magnet with no zero-field anomalous Hall effect, and is known to exhibit an in-plane magnetization ground state with complex spin textures leading to skyrmions and topological Hall effects[42–44]. Although this situation does not ideally match with a kagome Chern magnet picture, its soft magnetism and electron correlation nature leads to giant and anisotropic spin–orbit tunability that is of great interest, which we discuss later[41,45–48]. Another concern is that most topological kagome magnets have a tin (Sn) atom in the centre of their kagome lattice unit, which could lead to additional hopping that affects the ideal kagome band structure.

An alternative family[49–51], RMn_6Sn_6 (where R is a rare-earth element), was then proposed to overcome these two problems. The large chemical pressure of a rare-earth element can push the Sn atom away from the kagome layer. In particular, the ferrimagnet $TbMn_6Sn_6$ stands out owing to its unique out-of-plane magnetization required for Chern magnetism (Fig. 2a). Scanning tunnelling spectroscopy shows that the manganese (Mn) kagome lattice exhibits distinct Landau quantization under a magnetic field, which features a spin-polarized Dirac dispersion with a Chern gap Δ = 34 meV and a Dirac Fermi energy E_D = 130 meV. This Landau quantization fan maps out the Chern-gapped Dirac dispersion, which agrees well with angle-resolved photoemission results of the occupied states. Furthermore, a topological edge state with substantially reduced quasiparticle scattering is detected at 130 meV, which is within the Chern gap. Similar to the detection of spectroscopic Landau quantization, the longitudinal transport detects topological quantum oscillations[51,52] (Fig. 2b, top) in RMn_6Sn_6. The quantum oscillation matches with the Dirac Fermi surface from spectroscopic probes[50], and shows a cyclotron mass that agrees with the spectroscopic data. The intrinsic anomalous Hall conductivity (Fig. 2b, bottom) per kagome layer is measured to be $\sigma_{xy} = 0.14e^2/h$, which agrees with the estimation of the Berry curvature contribution based on spectroscopic data $\sigma_{xy} = \Delta/(2E_D) \times e^2/h = 0.13e^2/h$. These quantitative spectroscopic transport agreements build up the bulk–boundary–Berry correspondence for the kagome Chern magnet (Fig. 2a). Owing to the strong out-of-plane magnetism and large Berry curvature from Dirac fermions with a Chern gap, $TbMn_6Sn_6$ exhibits zero-field anomalous Hall, anomalous Nernst and anomalous thermal Hall effects[51–53] (Fig. 2b, bottom). The charge–entropy scaling derived from this anomalous transverse transport goes beyond the Mott formula[54] and the Wiedemann–Franz law[55] for ordinary electrons, but can be described, interestingly, by the new scaling behaviour derived from Dirac fermions with a Chern gap, suggesting a topological behaviour consistent with spectroscopic observations[50,52].

Owing to the pristine kagome lattice structure, a kagome-type band structure and anomalous Hall effect are widely searched for and detected in RMn_6Sn_6 and closely related compounds[50,56–64]. The recently discovered RV_6Sn_6 presents a complementary case where the vanadium (V)-based kagome layer is paramagnetic[60] and the R layer can be magnetic, and their clean kagome-type band structure is well captured by photoemission experiments and explained by first principles. The diverse chemical compositions and magnetic structures of these materials naturally lead to large spin–orbit tunability of its topological electronic structure. For instance, the rare-earth element can act as a tuning knob of the Chern gap, which scales with the underlying de Gennes factor[51]. In another related ferromagnet, $LiMn_6Sn_6$, a larger anomalous Hall effect is identified, which is probably owing to a smaller Dirac Fermi energy[63]. As discussed in the fundamental concepts of kagome electrons, in-plane magnetization tends to close the Chern gap, leading to giant spin–orbit tunability with respect to different magnetization configurations. Such magnetization control has been discussed for the Fe_3Sn_2 system[41,45–48] and RMn_6Sn_6 systems[60,63,64] through spectroscopic and transport experiments. Another intriguing phenomenon is the detection of nematicity in Fe_3Sn_2 (refs. [41,45]).

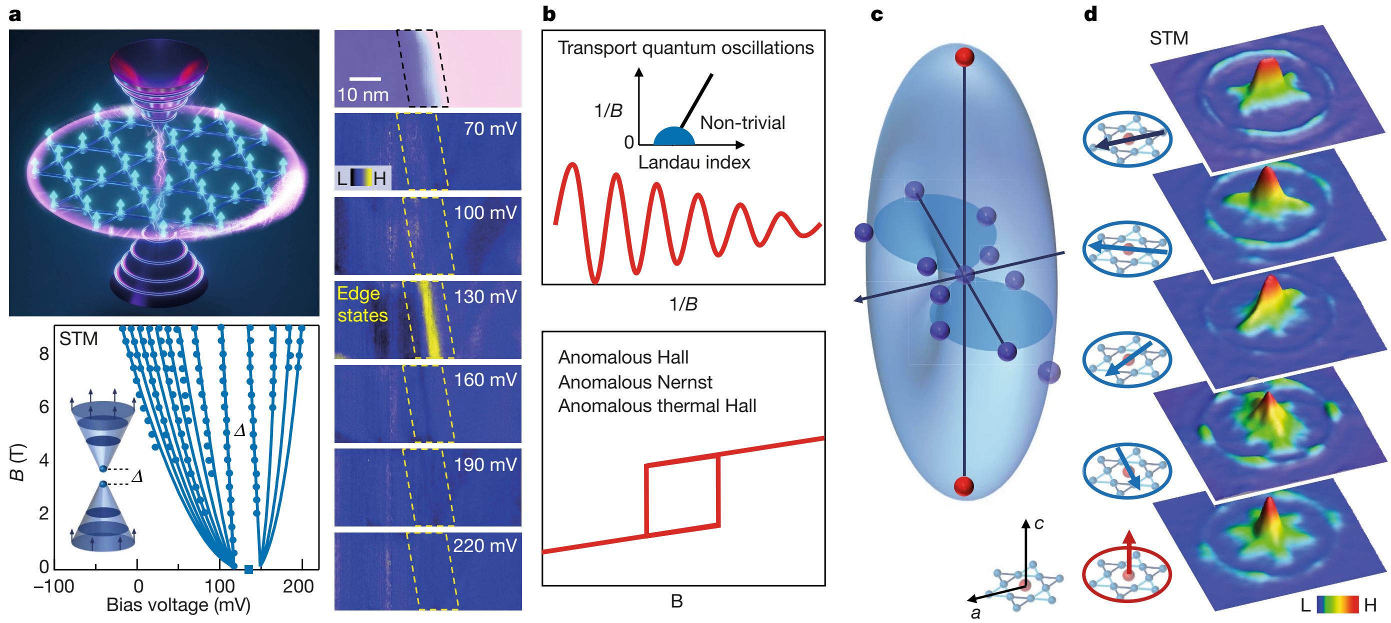

Fig. 2 | Chern quantum phase and spin–orbit tunability. a, Top-left: the features of a kagome Chern magnet $TbMn_6Sn_6$ in real space and momentum space (in each 2D kagome layer). In momentum space, spin-polarized Dirac fermions with a Chern energy gap (two separated cones) can exhibit Landau quantization. In real space, the spin–orbit-coupled magnetic kagome lattice (spheres with arrows pointing up) carries a topological edge state within the Chern energy gap. Bottom-left: the fitting of the Landau fan data (circles) with the spin-polarized and Chern-gapped Dirac dispersion (solid lines). Inset: schematic of Landau quantization of Chern-gapped Dirac fermions. Right: d*I*/d*V* maps (where *I* is the tunnelling current and *V* is the bias voltage) taken at different energies across a step edge (top). The map taken within the Chern gap energy (130 meV) shows a pronounced topological edge state. **b**, Topological transport signal for kagome Chern magnet $TbMn_6Sn_6$. Top: the longitudinal transport quantum oscillations as a function of inverse magnetic field $1/B$. Inset: the non-trivial Berry phase can be extracted from the intersection of the Landau index and $1/B = 0$, where the Landau index is extracted from the oscillation peaks. Bottom: the anomalous transverse transport as a function of magnetic field B. **c**, Vector-magnetization-induced energy shift of a quantum state in the topological kagome magnet Fe_3Sn_2. The light-blue surface shows a 3D illustration of the nematic energy shift ΔE as a function of the magnetization vector, which exhibits a nodal line along the *a* axis. **d**, Vector magnetization control of the electronic scattering in the topological kagome magnet Fe_3Sn_2. The electronic structure scattering patterns are shown as a function of the magnetization direction with respect to the kagome lattice, which is indicated in the insets. The topmost quasi-particle interference pattern shows the spontaneous nematicity along the *a* axis. Magnetization along other directions can alter, and, thus, control, the electronic scattering symmetry. In the colour bars, L denotes low and H denotes high on the intensity of the map. STM, scanning tunnelling microscopy. Panels adapted with permission from: **a**, ref. [50], Springer Nature Limited; **c**,**d**, ref. [41], Springer Nature Limited.

When rotating its magnetization along different in-plane directions, both the Zeeman energy shift and the quasiparticle scattering signal exhibit nematicity (two-fold symmetry; Fig. 2c,d), a hallmark of correlated electrons. The tunability of the kagome Chern magnets reveals a strong interplay between the exchange field or external magnetic field, electronic excitations and nematicity, providing ways to control the spin–orbit properties.

Weyl fermion and antiferromagnetic spintronics

Weyl fermions were first introduced in 1929 in the context of high-energy physics as massless particles with definite chirality, described by a two-component spinor obeying the Weyl equation[22]. Weyl fermions arise as low-energy quasiparticle excitations in 3D crystals lacking inversion symmetry or time-reversal symmetry[23,24,65,66]. In a Weyl crystal, Weyl fermions are the sources and sinks of the Berry curvature in momentum space (Fig. 3a). On its surface, a topological Fermi arc surface state is formed, which connects the projections of two Weyl points in the momentum space of the surface. The emergence of Weyl fermions in kagome magnets naturally requires strong interlayer coupling, such that the bulk electron bands are 3D. The non-collinear antiferromagnet Mn_3X (where X is Sn or Ge) and the ferromagnet $Co_3Sn_2S_2$ stand out[35–37,67–69], as the direct kagome lattice stacking in Mn_3X and strong ionic bonding through S^{2-} in $Co_3Sn_2S_2$ enhance the interlayer coupling. On the basis of the non-collinear in-plane antiferromagnetism[70] in Mn_3Sn and out-of-plane ferromagnetism[71] in $Co_3Sn_2S_2$, their Weyl fermions have been identified through theoretical calculations[35–37,68,69] (Fig. 3b). In these materials, unique negative magnetoresistance (Fig. 3c) has been reported, which is consistent with the expected chiral anomaly for Weyl fermions[36,69]. Meanwhile, certain features of the 2D kagome electrons are still traceable in their band structure, such as their kagome flat bands[72,73].

One remarkable property of Mn_3Sn is its room-temperature zero-field anomalous Hall effect[35] (and other related Berry curvature effects[74–80]) under a weak and soft magnetic moment, providing exceptional application value for antiferromagnetic spintronics[81]. For instance, in a bilayer device made with non-magnetic metals and an Mn_3Sn film, an electric current can manipulate the Hall voltage by switching the chiral kagome antiferromagnetism[78] (Fig. 3d). The electronic band dispersions of Mn_3X, however, have not been clearly detected, possibly owing to a strong electron correlation[69,73]. While similarly exhibiting giant anomalous Hall and related effects[36,37,82–88], $Co_3Sn_2S_2$ features a large ratio between anomalous Hall conductivity and longitudinal conductivity[36]. Such improvement is probably owing to its cleaner band structure that also enables better spectroscopic characterizations of its Weyl topology[82]. Guided by first-principles calculations, progress has progressively been made through counting the Chern numbers of the surface band crossings[83], imaging the linear band crossing with surface doping[84], imaging the diversity of quasiparticle interferences on surfaces hosting Fermi arcs[85], imaging the magnetic

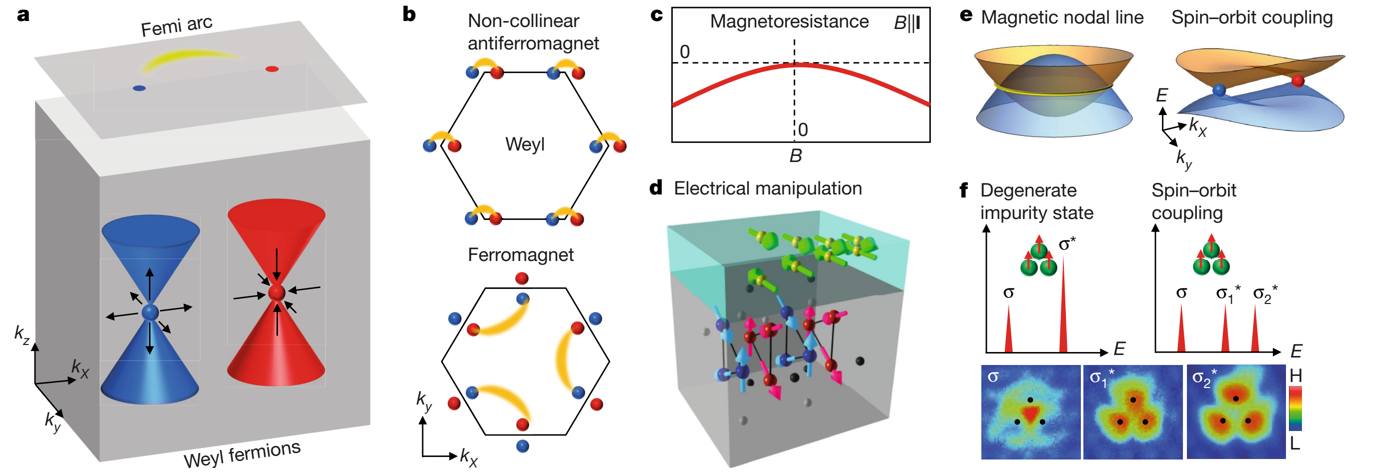

Fig. 3 | Weyl fermion and antiferromagnetic spintronics. a, Illustration of a pair of Weyl fermion quasiparticles with opposite chiral charges (red and blue spheres) in the 3D momentum space. The arrows illustrate the direction of the Berry curvature field in the vicinity of each Weyl fermion. The red and blue cones illustrate their respective linear Weyl dispersions in the bulk momentum space. On the top surface, a Fermi arc state (yellow arc) connects two Weyl cones in the surface momentum space. **b**, Illustration of Weyl Fermion positions and Fermi arc connectivity in the surface momentum space of the kagome non-collinear antiferromagnet Mn_3Sn (top) and the kagome ferromagnet $Co_3Sn_2S_2$ (bottom). Owing to the rotation-symmetry breaking of the non-colinear antiferromagnetism and spin–orbit coupling, the Weyl Fermion distribution and Fermi arc connectivity also break rotational symmetry. **c**, Negative magnetoresistance detected in Mn_3Sn and $Co_3Sn_2S_2$ that is consistent with the chiral anomaly expected for Weyl fermion quasiparticles. **d**, Electrical manipulation of the anomalous Hall effect for Mn_3Sn films (lower layer) through injecting current into non-magnetic metals (upper layer). **e**, Illustration of magnetic nodal line (yellow rings in the left image), and the spin–orbital-coupling-induced anisotropic splitting of the magnetic nodal ring (right image) that produces Weyl fermion quasiparticles (Weyl points at red and blue spheres). The blue and green shades illustrate the linear dispersion of the magnetic nodal line or Weyl cones in energy–momentum space. **f**, Real-space probe of the spin–orbit-coupling-induced quantum-state splitting in $Co_3Sn_2S_2$. Three interacting magnetic impurity states with C_{3v} geometry produce one bonding state σ and one doubly degenerate antibonding state σ* (top left). The spin–orbit coupling splits σ* into two states as $σ_1$* and $σ_2$* (top right), in analogy to the splitting of magnetic nodal line. The bottom panels show the real-space imaging of these three impurity-induced spin–orbit quantum states in $Co_3Sn_2S_2$. In the colour bars, L denotes low and H denotes high on the intensity of the map. Panels adapted with permission from: **d**, ref. [78], Springer Nature Limited; **f**, ref. [86], Springer Nature Limited.

phase transition of the topological band structure[87], and detecting the spin–orbit-coupling-induced energy gap[86,88].

We further clarify the relationship between the anomalous Hall effect and Weyl fermions. A pioneering study[89] of the anomalous Hall effect in Mn_3X-type materials attributes it to the Berry curvature effects from non-collinear magnetism without inviting the Weyl fermions. In magnetic crystals, there are generic magnetic nodal lines in the bulk bands protected by spinless mirror symmetry (Fig. 3e), and the spin–orbit coupling opens anisotropic gaps along the nodal lines, yielding nodes as pairs of Weyl cones. As one pair of Weyl fermions are often at the same energy acting as a source and a sink of Berry curvatures, respectively, their local integrated contribution to anomalous Hall conductivity essentially cancels out. However, the portions of the magnetic nodal lines that carry a large spin–orbit gap contribute to the integrated Berry curvature that leads to the anomalous Hall effect. This can be thought as a long-distance dipole effect of Weyl fermions[90], or as an effect of a local effective Chern gap. One initial evaluation of the spin–orbit gap in kagome Weyl magnets is to investigate the local geometrical impurity-induced resonances[86] (Fig. 3f). For triplet geometrical impurity-induced resonances, the spin–orbit coupling similarly breaks mirror symmetry to introduce a splitting gap[86], which is of a similar size to the magnetic nodal line gap[88].

Flat-band correlation and many-body physics

Kagome lattices host both high-velocity electrons (Dirac or Weyl fermions) and vanishing velocity electrons (flat band). Flat-band physics can be traced back to the fractional quantum Hall effect[25–27]. The Landau levels generated by a large magnetic field are perfect flat bands, and a fractional filling can produce the fractional quantum Hall effect with anyonic excitations. Without the magnetic field, flat bands are rare and emerge in only a few systems such as heavy-fermion compounds[91], kagome lattices (or line graphs[7,9]) and twisted bilayer graphene[92,93]. The paramagnet CoSn stands out owing to its simple crystal structure and cleaner flat bands in spectroscopic experiments, matching first-principles calculations[94–100]. The hallmark of a kagome flat band—quadratic band touching in momentum space (Fig. 4a)—is visualized by angle-resolved photoemission experiments[94,96]. As originally pointed out in the modelling of kagome electrons[20], the highly anisotropic *d* orbital can form flat bands. The *d* orbitals uniquely arrange themselves in the hexagonal ring of the kagome lattice (Fig. 4a, inset), leading to a nearly perfect cancelling of their propagating wavefunctions[96]. A similar arrangement of lattice vibration is found to produce localized phonon modes—flat-band phonons[95] (Fig. 4b).

The existence of flat bands leads to several emergent effects. The kagome flat bands have been known to favour ferromagnetism[1,7]. The flat bands in the ferromagnet Fe_3Sn_2 and the antiferromagnet FeSn can be related to their strong in-plane ferromagnetism[101–103]. With spin–orbit coupling, the quadratic degenerate points open a Z_2 topological gap (Fig. 4c), which is visualized in CoSn[94,96]. With the further introduction of out-of-plane ferromagnetism, it turns into a Chern gap, as in the flat-band case[72] of $Co_3Sn_2S_2$. The associated Berry curvature of this Chern gap leads to sizable orbital magnetism[104,105]. Tunnelling spectroscopy of the flat-band peak shifts anomalously with both positive and negative magnetic field[72], which goes beyond the conventional Zeeman effect. The anomalous Zeeman shift further supports the existence of orbital magnetism, with its direction being opposite to the bulk magnetization direction (Fig. 4c), which is consistent with the first-principles calculation[72]. Similar negative orbital magnetism physics is also detected for impurity resonances[86,106] as local flat bands in $Co_3Sn_2S_2$ and for anisotropic magnetic susceptibility[99] in CoSn. The negative orbital magnetism associated with Dirac fermions is also detected in a momentum-resolved way[61] in the antiferromagnet YMn_6Sn_6. Moreover, different from the bulk kagome flat band featuring

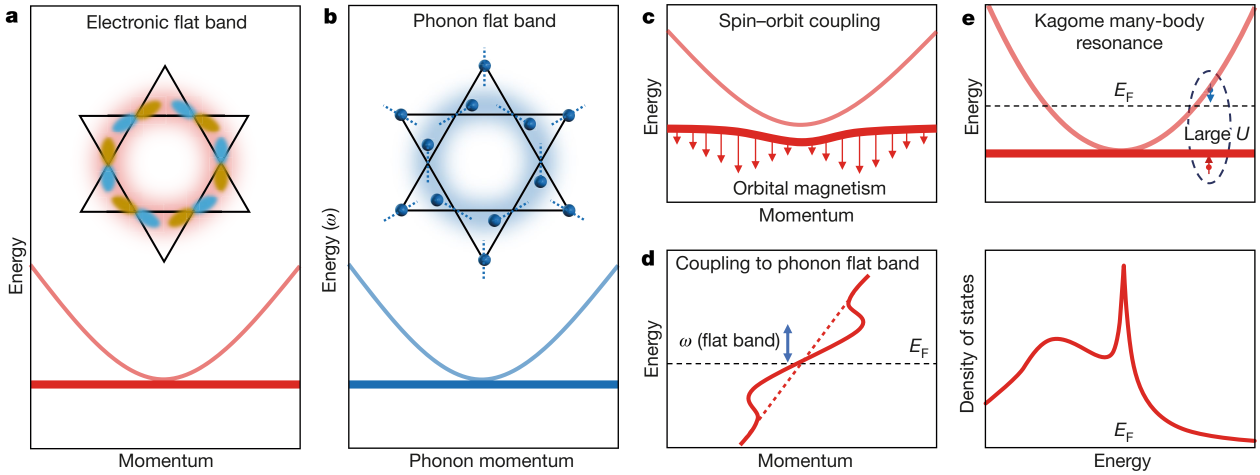

Fig. 4 | Flat-band correlation and many-body resonance. a, The electronic flat-band dispersion and how it touches a parabolic band without spin–orbit coupling, as detected in the kagome magnet $Co_3Sn_2S_2$ and the kagome paramagnet CoSn. Inset: the orbital configuration corresponding to the flat band in real space (the orbitals consider here are d_{xz} and d_{yz} orbitals from the top view). **b**, The phonon flat band and how it touches a parabolic band, as detected in CoSn. Inset: the lattice vibration distortion pattern corresponding to the phonon flat band (the dashed lines indicate the vibration directions of each atom). **c**, Spin–orbit coupling effects, which include a gap opening and negative orbital magnetism of the flat band that are detected in $Co_3Sn_2S_2$ and CoSn. **d**, Electronic structure coupling to the flat band phonon, as detected in CoSn. The electron band exhibits a double kink feature at the energy of the phonon flat band defined as ω. The electron–phonon coupling can lead to charge order and superconductivity instabilities. **e**, Many-body resonance owing to coupling of the flat band to the itinerant band under strong electron correlation (large U, as illustrated in the top panel) as detected in the kagome antiferromagnet Mn_3Sn. The bottom panel illustrates the Fano-shaped resonance in the density of states at Fermi energy, E_F.

a quadratic band touching, the surface flat band realized in FeSn does not have such a feature[103,107], and the realization of an atomic film of FeSn makes it an appealing platform for flat-band-based spintronic devices[108,109].

Besides the spin–orbit-driven topology, flat bands can lead to strong many-body interactions. The itinerant electrons in CoSn sense the strong coupling to its phonon flat band[95], leading to a kink in the band dispersion (Fig. 4d) and a peak–dip–hump structure in the tunnelling spectrum. The electron–phonon coupling can be a factor that leads to competing electronic instabilities that result in its paramagnetic state instead of ferromagnetism. In the kagome magnet Mn_3Sn, its electron correlation is substantially strong, as indicated by the large band renormalization factor[69]. Under this strong correlation, its single-particle flat band can couple to the itinerant electrons at the Fermi level, leading to a many-body resonance at the Fermi level[73] (Fig. 4e). The spectroscopic features of this many-body resonance, including Fano line shape and fast temperature broadening, resemble those detected in Kondo systems[91].

Unconventional charge-density waves

The interplay between topology and interaction has been extensively discussed for kagome superconductors. Although kagome superconductors with a transition temperature T_c up to 7 K have been known for over half a century (such as $CeRu_2$ and $LaRu_3Si_2$)[110–113], recently discovered kagome superconductors[114–117] AV_3Sb_5 (where A is K, Rb or Cs) show a charge-density wave[115,118,119], the ordering temperature T^* of which reaches 100 K. Above T^*, the band structure of AV_3Sb_5 features van Hove singularities at the Fermi level, and an indirect topological bandgap[115] under consideration of spin–orbit coupling. Both magnetization and transport measurements find an anomaly at T^*, which is considered to be a possible signature of orbital ordering[114] or a charge-density-wave-like instability[115]. Scanning tunnelling microscopy has identified the 2 × 2 in-plane supercells of the charge modulation, charge energy gap and charge-density reversal across the gap below T^*, which reveal a charge-density-wave order[118]. X-ray scattering has further identified 2 × 2× 2 3D supercells[119] below T^*. These initial experiments established the bulk 2 × 2 × 2 charge-density wave as the many-body state in the topological kagome superconductor AV_3Sb_5 below T^* (Fig. 5a), and its in-plane wavevector agrees with early studies of the possible electronic instability for kagome lattices[29,30]. A charge-density wave with similar 2 × 2 × 2 supercells has been detected in transition-metal dichalcogenides[120], and the chirality and the nematicity of the order have been discussed[120–123]. The antiphase coupling of the adjacent 2 × 2 order leads to nematicity in the first order and can feature chirality as a further orbital ordering[120–123]. Similar additional spatial symmetry breaking, as well as the associated lattice[124–134] and orbital[135–149] manifestations below the charge-density wave state of AV_3Sb_5, has been intensively investigated through various techniques[150]. Many of them connect with each other reasonably. For instance, tunnelling[118,136] and photoemission[142,146,147] show a consistent charge-density-wave gap for occupied states of ~20 meV (Fig. 5b). This systematic progress provides the fundamental concepts to understand the dual lattice–orbital nature of the charge-density wave in the kagome lattice.

An alternative paradigm for looking at the charge order focuses on its time-reversal symmetry breaking (Fig. 5c), which goes beyond the conventional charge-density wave and features orbital-current physics, as initially proposed for achieving the quantum anomalous Hall effect[15] and for the hidden phase in cuprates[32]. Pioneering magnetization[114], muon spin rotation[151] and tunnelling[118] studies have shown that both the phase transition temperature and the energy gap are insensitive to the magnetic field, and that there is no spin ordering. Thus, any magnetism should be a higher-order effect. One breakthrough is the detection of magnetic field switching of the 2 × 2 charge-order chirality[118,135,136], but regions with defects or strains featuring a much smaller energy gap do not show chirality[118,134–136]. The phenomenon of magnetic-field-controlled chirality can be modelled[118] by considering a relative phase between three sets of order parameters describing the charge order in the three kagome sublattices. This complex order parameter breaks time-reversal symmetry, leads to a large anomalous Hall effect[152,153] and introduces a small

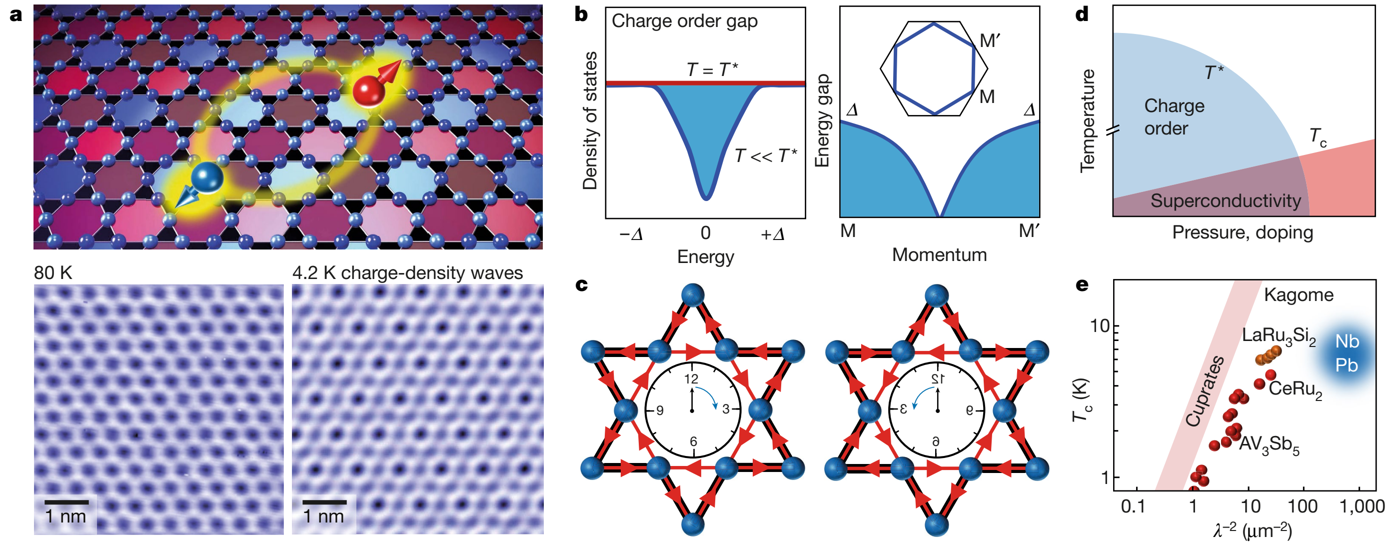

Fig. 5 | Charge-density wave and superconductivity. a, Top: schematic of the charge order and superconductivity detected in kagome superconductors AV_3Sb_5. The dark and light-blue spheres form the kagome lattice. The shade of the colour represents the unusual distribution pattern of the charge order. The large red and blue spheres with arrows represent Cooper pairing of the superconductivity. Bottom: an example of charge-order imaging. The topographic images are taken above (left) and below (right) the charge-ordering temperature T^* for the kagome superconductor KV_3Sb_5, where a 2 × 2 supercell of the charge order is identified. **b**, Charge-order gap in the density of states (left) and momentum electronic structure (right). A V-shaped charge-order gap opens at the Fermi level below T^* (left); in momentum space, the gap opens in an anisotropic way, with its maximum value at M or M′ (right; the inset shows the Fermi surface). **c**, Time-reversal-symmetry breaking of charge order in AV_3Sb_5 and the kagome antiferromagnet FeGe. The thick black lines mark the unit cell of the kagome charge order. The red arrows illustrate the orbital currents in the kagome lattice that breaks time-reversal symmetry. **d**, Physical-pressure- or chemical-doping-based phase diagram, showing the competition between charge order and superconductivity. **e**, Scaling plot for superconducting transition temperature T_C versus inverse squared magnetic penetration depth (λ^{-2}). The scaling relation for kagome superconductors (including $LaRu_3Si_2$, AV_3Sb_5 and $CeRu_2$) is close to that of cuprates but away from that of conventional superconductors such as Nb and Pb. Panel **a** adapted from ref. [118], Springer Nature Limited.

orbital magnetization. Theoretical studies[154–156] have uncovered that the time-reversal-symmetry-breaking charge order is energetically favourable in the kagome lattice close to the van Hove filling. This exotic charge order provides a rare example of many-body interaction-driven topology (Fig. 1f).

Magnetic-moment-sensitive probes[157–160], including muon spin rotation and Kerr rotation, further confirm the magnetic feature of the charge order. An external magnetic field can substantially boost the time-reversal-symmetry-breaking muon signal[157–159], providing insights beyond the initially considered magnetic-field insensitivity[114]. A recent observation of field-tuned chiral transport[161] further elaborated how spatial chirality and time-reversal-symmetry breaking twist with each other to introduce nonlinear magneto-transport, which is consistent with the spectroscopy detection of field-tuned electronic chirality[118,135,136]. In connection with a kagome superconductor, charge order is detected[162,163] in the kagome antiferromagnet FeGe. The essential physical picture of kagome charge order is further tested, including van-Hove-singularity-driven 2 × 2 charge instability, the anomalous contribution to the Hall effect, magnetic coupling of the charge order and internal exchange magnetic-field-tuned chirality switching. In addition, robust edge states are detected within the charge-order energy gap, which agrees with the topological nature of the time-reversal-symmetry-breaking charge order (Fig. 1f).

Magnetically intertwined superconductivity

Superconductivity in kagome lattices has long been identified to coexist with magnetic phases. One of the earliest known superconductors hosting a kagome lattice, $CeRu_2$, was termed as a ferromagnetic superconductor[110] by Matthias. The normal state of the kagome superconductor $CeRu_2$ is a weak magnet, probably owing to the flat-band correlation[110,111]. Coincidently, one early theory for kagome superconductors (Fig. 1g) predicts a time-reversal-symmetry-breaking superconducting ground state[33]. The intertwining between magnetism and superconductivity has also been theoretically considered for kagome electrons at the van Hove filling[28–30] and the Dirac filling[164]. These pioneering studies set the tone for exploring magnetically intertwined kagome superconductivity.

Applying this research theme to AV_3Sb_5, both physical pressure and chemical doping can suppress the charge order, while superconductivity is immediately enhanced[165–172], which indicates competition between the charge order and superconductivity (Fig. 5d). A question is whether the time-reversal symmetry is broken for superconductivity. An initial muon study argued that this symmetry breaking persists into superconductivity[157], as there is no additional relaxation rate change across T_c. This proposal is further substantiated by the observation of the relaxation rate change across T_c through killing the charge order by pressure tuning[158]. Further evidence for such intertwined physics comes from examining the effect of interactions affecting both the time-reversal-symmetry-breaking features of charge order and superconductivity. Theoretical analysis[30,154–156] indicates that the extended Coulomb interaction drives time-reversal-symmetry-breaking charge order. Owing to the poorly screened Coulomb interaction, the charge number fluctuations are suppressed. According to the number-phase uncertainty, quantum-phase fluctuations will proliferate leading to smaller superfluid density[173]. The penetration depth λ of several kagome superconductors has been measured[111,113,157–159], where λ^{-2} is proportional to the superfluid density, and suggests their small superfluid density. The scaling analysis of T_c versus λ^{-2} in these studies shows a marked difference from conventional superconductors but a close analogy to cuprates (Fig. 5e). The large T_c/λ^{-2} value attests to the unconventional nature of kagome superconductivity in the correlation sense, and implies a connection with the underlying interactions driving time-reversal-symmetry-breaking charge order.

In parallel, substantial research efforts[28–30,111,113,124,126,136,138,157,158,174–180] have also been devoted to determining the electron Cooper-pairing symmetry[150]. Experimentally, both nodeless and nodal superconducting gap structures, as well as their quantum tuning, have been reported. However, a direct momentum space determination of the pairing symmetry and topological order have been lacking. The topological nature of the superconducting state remains one of the active areas of investigation. Experiments have shown emergent features of the electron pairing, including the observation of a putative Majorana zero mode[124] and detection of pair density waves[126] on the kagome superconductor surface.

Future opportunities

With the rise in interest in quantum material studies[181], quantum interactions in topological kagome magnets and related superconductors have effectively bridged the research communities of correlated electrons and topological matter. This Review aims not to conclude this field but to invite further exploration and enjoyment of this quantum party held in the kagome lattice. At times, history mirrors the future. It is unlikely that in 2012, when substantial conceptual literature for kagome physics existed, we could have predicted the exciting discoveries reviewed here. However, this reflects the fast-growing nature of this field: it appears to be full of opportunities and seems to be progressing beyond projective expectations.

For kagome Chern magnets such as $TbMn_6Sn_6$ and similar materials, the corresponding monolayer or few-layer devices have not been successfully fabricated, which would allow for the demonstration of their cleaner electronic band structures and quantized transports. A first-principles-guided materials search towards more isolated or distinct kagome bands[20] is still needed for further development. One alternative route is to design and grow surface-supported metal–organic kagome frameworks[182,183]. For the kagome Weyl magnet Mn_3Sn, the experimental visualization of its Fermi arc and its vector magnetization control remain unsettled. Similarly, several kagome magnets exhibiting large transverse anomalous transport[184,185], including $UCo_{0.8}Ru_{0.2}Al$ and Fe_3Sn, still await spectroscopic visualization of their topological fermions. From the first-principles prediction[186] and microscopic studies of the bulk crystal's surface edge[187] of monolayer $Co_3Sn_2S_2$, it is expected to exhibit a Chern insulator phase, which awaits experimental realization. The realization of monolayer or few-layer kagome magnets would also be a significant step towards the prediction of a high-temperature fractional Chern insulator phase[19], which requires an isolated flat Chern band with strong interaction and electrical tunability. An opportunity has been provided by computational advances in building a catalogue of flat-band stoichiometric materials[188]. Moreover, the Landau level of spin–orbit-coupled kagome flat bands has recently been shown to be highly unconventional[189]. The high-energy-resolution- and high-magnetic-field-based spectroscopic mapping of the Landau fan of the kagome flat band in $Co_3Sn_2S_2$ and CoSn can serve as a promising tool for testing this theoretical modelling. The identification[162,163] of a charge-density wave in FeGe is encouraging for the search of charge order in more topological kagome magnets. In parallel, as charge order can be a precursor of superconductivity, it is also meaningful to further engineer FeGe with chemical doping and pressure to look for superconductivity. In the kagome superconductor AV_3Sb_5, electronic evidence for a time-reversal-symmetry-breaking superconducting state has been lacking. The search for time-reversal-symmetry-breaking superconductivity with odd parity pairing may allow us to realize intrinsic topological superconductivity in either 3D or monolayer/few-layer kagome materials with a sizable gap, and the bulk Majorana zero modes and chiral Majorana edge states thus open a route to exploring the quantum information frontier[190,191].

Although the above questions are of current interest, there are longer-term explorative directions. For instance, it has long been proposed that kagome lattice systems are promising for the realization of gapped or Dirac spin liquids[192,193]. The existence of time-reversal-symmetry breaking in realistic materials may also facilitate the possibility of a chiral spin liquid[194,195] with detectable quantized transport[196,197]. The doped kagome quantum spin liquid can become an exotic superconductor[33], and may give rise to more unknown phases in mixing the quantum spin liquid and the superconducting state. In addition, doped kagome herbertsmithite systems can host strongly correlated Dirac fermions[164], and have recently been proposed to realize viscous electron fluids that can be described by holography to make a possible model for quantum connection to gravity[198]. Moreover, kagome physics may occur in moiré systems that are highly tunable. For example, a twisted kagome lattice bilayer can yield emergent flat bands[199] similar to that in magic-angle twisted bilayer graphene. On the contrary, the twisted graphene system is also predicted to be able to produce kagome electronic bands[200], which may allow the realization of pristine kagome electrons without spin–orbital coupling and related interaction-driven phases. Although existing research in quantum materials remains largely within the interplay of the quantum (anomalous) Hall effect and (unconventional) superconductivity, we look forward to reaching a regime of 'unknown unknowns' with the next generation of cleaner and artificial kagome materials.

1. Syôzi, I. Statistics of kagomé lattice. *Prog. Theor. Phys.* **6**, 306–308 (1951).
Introduction of the kagome lattice to quantum physics.
2. Onsager, L. et al. Crystal statistics. I. A two-dimensional model with an order–disorder transition. *Phys. Rev.* **65**, 117–149 (1944).
3. Anderson, P. W. Resonating valence bonds: a new kind of insulator? *Mater. Res. Bull.* **8**, 153–160 (1973).
4. Broholm, C. et al. Quantum spin liquids. *Science* **367**, eaay0668 (2020).
5. Heisenberg, W. Zur Theorie des Ferromagnetismus. *Z. Phys.* **49**, 619–636 (1928).
6. Stoner, E. C. Collective electron ferromagnetism. *Proc. R. Soc. Lond. Ser. A* **165**, 372–414 (1938).
7. Mielke, A. Ferromagnetic ground states for the Hubbard model on line graphs. *J. Phys. A* **24**, L73 (1991).
Identification of electronic structure in a kagome lattice.
8. Anderson, P. W. More is different. *Science* **177**, 393–396 (1972).
9. Lieb, E. H. Two theorems on the Hubbard model. *Phys. Rev. Lett.* **62**, 1201–1204 (1989).
10. Hasan, M. Z. & Kane, C. L. Colloquium: Topological insulators. *Rev. Mod. Phys.* **82**, 3045–3067 (2010).
11. Qi, X.-L. & Zhang, S.-C. Topological insulators and superconductors. *Rev. Mod. Phys.* **83**, 1057–1110 (2011).
12. Hasan, M. Z., Xu, S.-Y. & Bian, G. Topological insulators, topological superconductors and Weyl fermion semimetals: discoveries, perspectives and outlooks. *Phys. Scr.* **2015**, 014001 (2015).
13. Keimer, B., Kivelson, S., Norman, M., Uchida, M. & Zaanen, J. From quantum matter to high-temperature superconductivity in copper oxides. *Nature* **518**, 179–186 (2015).
14. Ohgushi, K., Murakami, S. & Nagaosa, N. Spin anisotropy and quantum Hall effect in the kagomé lattice: chiral spin state based on a ferromagnet. *Phys. Rev. B* **62**, R6065 (2000).
15. Haldane, F. D. M. Model for a quantum Hall effect without Landau levels: condensed matter realization of the "parity anomaly". *Phys. Rev. Lett.* **61**, 2015–2018 (1988).
16. Kane, C. L. & Mele, E. J. Quantum spin Hall effect in graphene. *Phys. Rev. Lett.* **95**, 226801 (2005).
17. Bernevig, B. A., Hughes, T. L. & Zhang, S. C. Quantum spin Hall effect and topological phase transition in HgTe quantum wells. *Science* **314**, 1757–1761 (2006).
18. Guo, H. M. & Franz, M. Topological insulator on the kagome lattice. *Phys. Rev. B* **80**, 113102 (2009).
19. Tang, E., Mei, J. W. & Wen, X. G. High-temperature fractional quantum Hall states. *Phys. Rev. Lett.* **106**, 236802 (2011).
20. Xu, G., Lian, B. & Zhang, S.-C. Intrinsic quantum anomalous Hall effect in the kagome lattice $Cs_2LiMn_3F_{12}$. *Phys. Rev. Lett.* **115**, 186802 (2015).
Prediction of a kagome Chern magnet.
21. Halperin, B. I. Possible states for a three-dimensional electron gas in a strong magnetic field. *Jpn J. Appl. Phys.* **26**, 1913–1919 (1987).
22. Weyl, H. Elektron und gravitation. *I. Z. Phys.* **56**, 330–352 (1929).
23. Wan, X., Turner, A. M., Vishwanath, A. & Savrasov, S. Y. Topological semimetal and Fermi-arc surface states in the electronic structure of pyrochlore iridates. *Phys. Rev. B* **83**, 205101 (2011).
24. Burkov, A. A. & Balents, L. Weyl semimetal in a topological insulator multilayer. *Phys. Rev. Lett.* **107**, 127205 (2011).
25. Tsui, D. C., Stormer, H. L. & Gossard, A. C. Two-dimensional magnetotransport in the extreme quantum limit. *Phys. Rev. Lett.* **48**, 1559–1562 (1982).
26. Laughlin, R. B. Anomalous quantum Hall effect: an incompressible quantum fluid with fractionally charged excitations. *Phys. Rev. Lett.* **50**, 1395–1398 (1983).
27. Qi, X.-L. Generic wave-function description of fractional quantum anomalous Hall states and fractional topological insulators. *Phys. Rev. Lett.* **107**, 126803 (2011).
28. Yu, S.-L. & Li, J.-X. Chiral superconducting phase and chiral spin-density-wave phase in a Hubbard model on the kagome lattice. *Phys. Rev. B* **85**, 144402 (2012).

29. Wang, W.-S., Li, Z.-Z., Xiang, Y.-Y. & Wang, Q.-H. Competing electronic orders on kagome lattices at van Hove filling. *Phys. Rev. B* **87**, 115135 (2013).
30. Kiesel, M. L., Platt, C. & Thomale, R. Unconventional Fermi surface instabilities in the kagome Hubbard model. *Phys. Rev. Lett.* **110**, 126405 (2013).
31. Zhu, W., Gong, S.-S., Zeng, T.-S., Fu, L. & Sheng, D. S. Interaction-driven spontaneous quantum Hall effect on a kagome lattice. *Phys. Rev. Lett.* **117**, 096402 (2016).
32. Varma, C. M. Non-Fermi-liquid states and pairing instability of a general model of copper oxide metals. *Phys. Rev. B* **55**, 14554–14580 (1997).
33. Ko, W.-H., Lee, P. A. & Wen, X.-G. Doped kagome system as exotic superconductor. *Phys. Rev. B* **79**, 214502 (2009).
Prediction of time-reversal-symmetry-breaking kagome superconductivity.
34. Kida, T. et al. The giant anomalous Hall effect in the ferromagnet Fe_3Sn_2—a frustrated kagome metal. *J. Phys. Condens. Matter* **23**, 112205 (2011).
Observation of giant anomalous Hall effect in a kagome ferromagnet.
35. Nakatsuji, S., Kiyohara, N. & Higo, T. Large anomalous Hall effect in a noncollinear antiferromagnet at room temperature. *Nature* **527**, 212–215 (2015).
Observation of room-temperature giant anomalous Hall effect in a kagome antiferromagnet.
36. Liu, E. et al. Giant anomalous Hall effect in a ferromagnetic kagome-lattice semimetal. *Nat. Phys.* **14**, 1125–1131 (2018).
37. Wang, Q. et al. Large intrinsic anomalous Hall effect in half-metallic ferromagnet $Co_3Sn_2S_2$ with magnetic Weyl fermions. *Nat. Commun.* **9**, 3681 (2018).
38. Nagaosa, N., Sinova, J., Onoda, S., MacDonald, A. H. & Ong, N. P. Anomalous Hall effect. *Rev. Mod. Phys.* **82**, 1539–1592 (2010).
39. Chang, C. Z. et al. Experimental observation of the quantum anomalous Hall effect in a magnetic topological insulator. *Science* **340**, 167–170 (2013).
40. Ye, L. et al. Massive Dirac fermions in a ferromagnetic kagome metal. *Nature* **555**, 638–642 (2018).
Observation of massive Dirac fermions in a kagome ferromagnetic metal.
41. Yin, J. X. et al. Giant and anisotropic many-body spin–orbit tunability in a strongly correlated kagome magnet. *Nature* **562**, 91–95 (2018).
Observation of spin–orbit tunability, Berry curvature response and electronic nematicity in a kagome magnet.
42. Fenner, L. A., Dee, A. A. & Wills, A. S. Non-collinearity and spin frustration in the itinerant kagome ferromagnet Fe_3Sn_2. *J. Phys. Condens. Matter* **21**, 452202 (2009).
43. Hou, Z. et al. Observation of various and spontaneous magnetic skyrmionic bubbles at room temperature in a frustrated kagome magnet with uniaxial magnetic anisotropy. *Adv. Mater.* **29**, 1701144 (2017).
44. Wang, Q., Yin, Q. & Lei, H. Giant topological Hall effect of ferromagnetic kagome metal Fe_3Sn_2. *Chin. Phys. B* **29**, 017101 (2020).
45. Li, Y. et al. Magnetic-field control of topological electronic response near room temperature in correlated kagome magnets. *Phys. Rev. Lett.* **123**, 196604 (2019).
46. Ye, L. et al. de Haas–van Alphen effect of correlated Dirac states in kagome metal Fe_3Sn_2. *Nat. Commun.* **10**, 4870 (2019).
47. Tanaka, H. et al. Three-dimensional electronic structure in ferromagnetic Fe_3Sn_2 with breathing kagome bilayers. *Phys. Rev. B* **101**, 161114(R) (2020).
48. Fang, S. Ferromagnetic helical nodal line and Kane–Mele spin–orbit coupling in kagome metal Fe_3Sn_2. *Phys. Rev. B* **105**, 035107 (2022).
49. Venturini, G., ElIdrissi, B. C. & Malaman, B. Magnetic properties of RMn_6Sn_6 (R = Sc, Y, Gd–Tm, Lu) compounds with $HfFe_6Ge_6$ type structure. *J. Magn. Magn. Mater.* **94**, 35–42 (1991).
50. Yin, J.-X. et al. Quantum-limit Chern topological magnetism in $TbMn_6Sn_6$. *Nature* **583**, 533–536 (2020).
Observation of a quantum-limit kagome Chern magnet with topological edge state.
51. Ma, W. et al. Rare earth engineering in RMn_6Sn_6 (R = Gd–Tm, Lu) topological kagome magnets. *Phys. Rev. Lett.* **126**, 246602 (2021).
52. Xu, X. et al. Topological charge–entropy scaling in kagome Chern magnet $TbMn_6Sn_6$. *Nat. Commun.* **13**, 1197 (2022).
53. Zhang, H. et al. Exchange-biased topological transverse thermoelectric effects in a kagome ferrimagnet. *Nat. Commun.* **13**, 1091 (2022).
54. Mott, N. F. et al. *The Theory of the Properties of Metals and Alloys* (Courier Dover Publications, 1958).
55. Wiedemann, G. & Franz, R. Relative conductivity of solids. *Ann. Phys. Chem.* **89**, 497–531 (1853).
56. Asaba, T. et al. Anomalous Hall effect in the kagome ferrimagnet $GdMn_6Sn_6$. *Phys. Rev. B* **101**, 174415 (2020).
57. Ghimire, N. J. et al. Competing magnetic phases and fluctuation-driven scalar spin chirality in the kagome metal YMn_6Sn_6. *Sci. Adv.* **6**, eabe2680 (2020).
58. Li, M. et al. Dirac cone, flat band and saddle point in kagome magnet YMn_6Sn_6. *Nat. Commun.* **12**, 3129 (2021).
59. Wang, Q. et al. Field-induced topological Hall effect and double-fan spin structure with a c-axis component in the metallic kagome antiferromagnetic compound YMn_6Sn_6. *Phys. Rev. B* **103**, 014416 (2021).
60. Peng, S. et al. Realizing kagome band structure in two-dimensional kagome surface states of RV_6Sn_6 (R=Gd, Ho). *Phys. Rev. Lett.* **127**, 266401 (2021).
61. Li, H. et al. Manipulation of Dirac band curvature and momentum-dependent *g* factor in a kagome magnet. *Nat. Phys.* **18**, 644–649 (2022).
Momentum-resolved *g* factor in a kagome antiferromagnet.
62. Riberolles, S. X. M. et al. Low temperature competing magnetic energy scales in the topological ferrimagnet $TbMn_6Sn_6$. *Phys. Rev. X* **12**, 021043 (2022).
63. Chen, D. et al. Large anomalous Hall effect in the kagome ferromagnet $LiMn_6Sn_6$. *Phys. Rev. B* **103**, 144410 (2021).
64. Siegfried, P. E. et al. Magnetization-driven Lifshitz transition and charge-spin coupling in the kagome metal YMn_6Sn_6. *Commun. Phys.* **5**, 58 (2022).
65. Armitage, N. P., Mele, E. J. & Vishwanath, A. Weyl and Dirac semimetals in three-dimensional solids. *Rev. Mod. Phys.* **90**, 015001 (2018).
66. Hasan, M. Z. et al. Weyl, Dirac and high-fold chiral fermions in topological quantum matter. *Nat. Rev. Mater.* **6**, 784–803 (2021).
67. Nayak, A. K. et al. Large anomalous Hall effect driven by a nonvanishing Berry curvature in the noncolinear antiferromagnet Mn_3Ge. *Sci. Adv.* **2**, e1501870 (2016).
68. Yang, H. et al. Topological Weyl semimetals in the chiral antiferromagnetic materials Mn_3Ge and Mn_3Sn. *New J. Phys.* **19**, 015008 (2017).
Prediction of kagome Weyl materials.
69. Kuroda, K. et al. Evidence for magnetic Weyl fermions in a correlated metal. *Nat. Mater.* **16**, 1090–1095 (2017).
70. Tomiyoshi, S. & Yamaguchi, Y. Magnetic structure and weak ferromagnetism of Mn_3Sn studied by polarized neutron diffraction. *J. Phys. Soc. Jpn* **51**, 2478–2486 (1982).
71. Weihrich, R., Anusca, I. & Zabel, M. Half-antiperovskites: structure and type–antitype relations of shandites $M_{3/2}As$ (M = Co, Ni; A = In, Sn). *Z. Anorg. Allg. Chem.* **631**, 1463–1470 (2005).
72. Yin, J.-X. et al. Negative flat band magnetism in a spin–orbit-coupled correlated kagome magnet. *Nat. Phys.* **15**, 443–448 (2019).
Observation of topological flat-band and orbital magnetization in a kagome magnet.
73. Zhang, S. S. et al. Many-body resonance in a correlated topological kagome antiferromagnet. *Phys. Rev. Lett.* **125**, 046401 (2020).
Observation of many-body resonance in a topological kagome magnet.
74. Ikhlas, M. et al. Large anomalous Nernst effect at room temperature in a chiral antiferromagnet. *Nat. Phys.* **13**, 1085–1090 (2017).
75. Li, X. et al. Anomalous Nernst and Righi–Leduc effects in Mn_3Sn: Berry curvature and entropy flow. *Phys. Rev. Lett.* **119**, 056601 (2017).
76. Higo, T. et al. Large magneto-optical Kerr effect and imaging of magnetic octupole domains in an antiferromagnetic metal. *Nat. Photon* **12**, 73–78 (2018).
77. Kimata, M. et al. Magnetic and magnetic inverse spin Hall effects in a non-collinear antiferromagnet. *Nature* **565**, 627–630 (2019).
78. Tsai, H. et al. Electrical manipulation of a topological antiferromagnetic state. *Nature* **580**, 608–613 (2020).
Proposal for spintronic application of a kagome Weyl magnet.
79. Xu, L. et al. Finite-temperature violation of the anomalous transverse Wiedemann–Franz law. *Sci. Adv.* **6**, eaaz3522 (2020).
80. Chaudhary, G., Burkov, A. A. & Heinonen, O. G. Magnetism and magnetotransport in the kagome antiferromagnet Mn_3Ge. *Phys. Rev. B* **105**, 085108 (2022).
81. Baltz, V. et al. Antiferromagnetic spintronics. *Rev. Mod. Phys.* **90**, 015005 (2018).
82. Bernevig, B. A., Felser, C. & Beidenkopf, H. Progress and prospects in magnetic topological materials. *Nature* **603**, 41–51 (2022).
83. Guguchia, Z. et al. Tunable anomalous Hall conductivity through volume-wise magnetic competition in a topological kagome magnet. *Nat. Commun.* **11**, 559 (2020).
84. Liu, D. F. et al. Magnetic Weyl semimetal phase in a kagomé crystal. *Science* **365**, 1282–1285 (2019).
85. Morali, N. et al. Fermi-arc diversity on surface terminations of the magnetic Weyl semimetal $Co_3Sn_2S_2$. *Science* **365**, 1286–1291 (2019).
Quasiparticle scattering of the surface Fermi arc states in a kagome magnet.
86. Yin, J.-X. et al. Spin–orbit quantum impurity in a topological magnet. *Nat. Commun.* **11**, 4415 (2020).
87. Belopolski, I. et al. Signatures of Weyl fermion annihilation in a correlated kagome magnet. *Phys. Rev. Lett.* **127**, 256403 (2021).
88. Liu, D. et al. Direct observation of the spin–orbit coupling effect in magnetic Weyl semimetal $Co_3Sn_2S_2$. *npj Quantum Mater.* **7**, 11 (2022).
Momentum-resolved spin–orbit gap in a kagome Weyl magnet.
89. Chen, H., Niu, Q. & MacDonald, A. H. Anomalous Hall effect arising from noncollinear antiferromagnetism. *Phys. Rev. Lett.* **112**, 017205 (2014).
90. Burkov, A. A. Anomalous Hall effect in Weyl metals. *Phys. Rev. Lett.* **113**, 187202 (2014).
91. Si, Q. & Steglich, F. Heavy fermions and quantum phase transitions. *Science* **329**, 1161–1166 (2010).
92. Bistritzer, R. & MacDonald, A. H. Moiré bands in twisted double-layer graphene. *Proc. Natl Acad. Sci. USA* **108**, 12233–12237 (2011).
93. Cao, Y. et al. Unconventional superconductivity in magic-angle graphene superlattices. *Nature* **556**, 43–50 (2018).
94. Liu, Z. H. et al. Orbital-selective Dirac fermions and extremely flat bands in frustrated kagome-lattice metal CoSn. *Nat. Commun.* **11**, 4002 (2020).
95. Yin, J. X. et al. Fermion–boson many-body interplay in a frustrated kagome paramagnet. *Nat. Commun.* **11**, 4003 (2020).
96. Kang, M. et al. Topological flat bands in frustrated kagome lattice CoSn. *Nat. Commun.* **11**, 4004 (2020).
97. Meier, W. R. et al. Flat bands in the CoSn-type compounds. *Phys. Rev. B* **102**, 075148 (2020).
98. Xie, Y. et al. Spin excitations in metallic kagome lattice FeSn and CoSn. *Commun. Phys.* **4**, 240 (2021).
99. Huang, H. et al. Flat-band-induced anomalous anisotropic charge transport and orbital magnetism in kagome metal CoSn. *Phys. Rev. Lett.* **128**, 096601 (2022).
100. Wan, S., Lu, H. & Huang, L. Temperature dependence of correlated electronic states in the archetypal kagome metal CoSn. *Phys. Rev. B* **105**, 155131 (2022).
101. Lin, Z. et al. Flatbands and emergent ferromagnetic ordering in Fe_3Sn_2 kagome lattices. *Phys. Rev. Lett.* **121**, 096401 (2018).
Kagome flat-band-induced emergent ferromagnetism.
102. Sales, B. C. et al. Electronic, magnetic, and thermodynamic properties of the kagome layer compound FeSn. *Phys. Rev. Mater.* **3**, 114203 (2019).
103. Kang, M. et al. Dirac fermions and flat bands in the ideal kagome metal FeSn. *Nat. Mater.* **19**, 163–169 (2020).
104. Karplus, R. & Luttinger, J. M. Hall effect in ferromagnetics. *Phys. Rev.* **95**, 1154–1160 (1954).
105. Vanderbilt, D. in *Electronic Structure Theory: Electric Polarization, Orbital Magnetization and Topological Insulators* (Cambridge Univ. Press, 2018).
106. Xing, Y. et al. Localized spin–orbit polaron in magnetic Weyl semimetal $Co_3Sn_2S_2$. *Nat. Commun.* **11**, 5613 (2020).
107. Lin, Z. et al. Dirac fermions in antiferromagnetic FeSn kagome lattices with combined space inversion and time-reversal symmetry. *Phys. Rev. B* **102**, 155103 (2020).

108. Inoue, H. et al. Molecular beam epitaxy growth of antiferromagnetic kagome metal FeSn. *Appl. Phys. Lett.* **115**, 072403 (2019).
109. Han, M. et al. Evidence of two-dimensional flat band at the surface of antiferromagnetic kagome metal FeSn. *Nat. Commun.* **12**, 5345 (2021).
110. Matthias, B. T., Suhl, H. & Corenzwit, E. Ferromagnetic superconductors. *Phys. Rev. Lett.* **1**, 449 (1958).
111. Mielke, C. III et al. Local spectroscopic evidence for a nodeless magnetic kagome superconductor $CeRu_2$. *J. Phys. Condens. Matter* **34**, 485601 (2022).
112. Ku, H. C., Meisner, G. P., Acker, F. & Johnston, D. C. Superconducting and magnetic properties of new ternary borides with the $CeCo_3B_2$-type structure. *Solid State Commun.* **35**, 91 (1980).
113. Mielke, C.III. et al. Nodeless kagome superconductivity in $LaRu_3Si_2$. *Phys. Rev. Mater.* **5**, 034803 (2021).
114. Ortiz, B. R. et al. New kagome prototype materials: discovery of KV_3Sb_5, RbV_3Sb_5, and CsV_3Sb_5. *Phys. Rev. Mater.* **3**, 094407 (2019).
115. Ortiz, B. R. et al. CsV_3Sb_5: a Z_2 topological kagome metal with a superconducting ground state. *Phys. Rev. Lett.* **125**, 247002 (2020).
Observation of superconductivity in AV_3Sb_5 compounds.
116. Ortiz, B. R. et al. Superconductivity in the Z_2 kagome metal KV_3Sb_5. *Phys. Rev. Mater.* **5**, 034801 (2021).
117. Yin, Q. et al. Superconductivity and normal-state properties of kagome metal RbV_3Sb_5 single crystals. *Chin. Phys. Lett.* **38**, 037403 (2021).
118. Jiang, Y. X. et al. Unconventional chiral charge order in kagome superconductor KV_3Sb_5. *Nat. Mater.* **20**, 1353–1357 (2021).
Observation of 2×2 charge-density-wave order with magnetic response in a kagome superconductor.
119. Li, H. et al. Observation of unconventional charge density wave without acoustic phonon anomaly in kagome superconductors AV_3Sb_5 (A=Rb, Cs). *Phys. Rev. X* **11**, 031050 (2021).
120. Ishioka, J. et al. Chiral charge-density waves. *Phys. Rev. Lett.* **105**, 176401 (2010).
121. van Wezel, J. Chirality and orbital order in charge density waves. *Europhys. Lett.* **96**, 67011 (2011).
122. Hildebrand, B. et al. Local real-space view of the achiral 1T-$TiSe_2$ 2×2×2 charge density wave. *Phys. Rev. Lett.* **120**, 136404 (2018).
123. Xu, S. Y. et al. Spontaneous gyrotropic electronic order in a transition-metal dichalcogenide. *Nature* **578**, 545–549 (2020).
124. Liang, Z. et al. Three-dimensional charge density wave and surface-dependent vortex-core states in a kagome superconductor CsV_3Sb_5. *Phys. Rev. X* **11**, 031026 (2021).
125. Zhao, H. et al. Cascade of correlated electron states in a kagome superconductor CsV_3Sb_5. *Nature* **599**, 216–221 (2021).
126. Chen, H. et al. Roton pair density wave in a strong-coupling kagome superconductor. *Nature* **599**, 222–228 (2021).
Observation of pair density wave in a kagome superconductor.
127. Tan, H., Liu, Y., Wang, Z. & Yan, B. Charge density waves and electronic properties of superconducting kagome metals. *Phys. Rev. Lett.* **127**, 046401 (2021).
128. Miao, H. et al. Geometry of the charge density wave in the kagome metal AV_3Sb_5. *Phys. Rev. B* **104**, 195132 (2021).
129. Ratcliff, N. et al. Coherent phonon spectroscopy and interlayer modulation of charge density wave order in the kagome metal CsV_3Sb_5. *Phys. Rev. Mater.* **5**, L111801 (2021).
130. Uykur, E. et al. Optical detection of the density-wave instability in the kagome metal KV_3Sb_5. *npj Quantum Mater.* **7**, 16 (2022).
131. Xie, Y. et al. Electron–phonon coupling in the charge density wave state of CsV_3Sb_5. *Phys. Rev. B* **105**, L140501 (2022).
132. Liu, G. et al. Observation of anomalous amplitude modes in the kagome metal CsV_3Sb_5. *Nat. Commun.* **13**, 3461 (2022).
133. Luo, J. et al. Possible star-of-David pattern charge density wave with additional modulation in the kagome superconductor CsV_3Sb_5. *npj Quantum Mater.* **7**, 30 (2022).
134. Li, H. et al. Rotation symmetry breaking in the normal state of a kagome superconductor KV_3Sb_5. *Nat. Phys.* **18**, 265–270 (2022).
135. Shumiya, N. et al. Intrinsic nature of chiral charge order in the kagome superconductor RbV_3Sb_5. *Phys. Rev. B* **104**, 035131 (2021).
136. Wang, Z. et al. Electronic nature of chiral charge order in the kagome superconductor CsV_3Sb_5. *Phys. Rev. B* **104**, 075148 (2021).
137. Ortiz, B. R. et al. Fermi surface mapping and the nature of charge-density-wave order in the kagome superconductor CsV_3Sb_5. *Phys. Rev. X* **11**, 041030 (2021).
138. Ni, S. et al. Anisotropic superconducting properties of kagome metal CsV_3Sb_5. *Chin. Phys. Lett.* **38**, 057403 (2021).
139. Xiang, Y. et al. Twofold symmetry of *c*-axis resistivity in topological kagome superconductor CsV_3Sb_5 with in-plane rotating magnetic field. *Nat. Commun.* **12**, 6727 (2021).
140. Nie, L. et al. Charge-density-wave-driven electronic nematicity in a kagome superconductor. *Nature* **604**, 59–64 (2022).
141. Liu, Z. et al. Charge-density-wave-induced bands renormalization and energy gaps in a kagome superconductor RbV_3Sb_5. *Phys. Rev. X* **11**, 041010 (2021).
142. Nakayama, K. et al. Multiple energy scales and anisotropic energy gap in the charge-density-wave phase of the kagome superconductor CsV_3Sb_5. *Phys. Rev. B* **104**, L161112 (2021).
143. Cho, S. et al. Emergence of new van Hove singularities in the charge density wave state of a topological kagome metal RbV_3Sb_5. *Phys. Rev. Lett.* **127**, 236401 (2021).
144. Park, T., Ye, M. & Balents, L. Electronic instabilities of kagome metals: saddle points and Landau theory. *Phys. Rev. B* **104**, 035142 (2021).
145. Christensen, M. H., Birol, T., Andersen, B. M. & Fernandes, R. M. Theory of the charge density wave in AV_3Sb_5 kagome metals. *Phys. Rev. B* **104**, 214513 (2021).
146. Luo, H. et al. Electronic nature of charge density wave and electron–phonon coupling in kagome superconductor KV_3Sb_5. *Nat. Commun.* **13**, 273 (2022).
147. Kang, M. et al. Twofold van Hove singularity and origin of charge order in topological kagome superconductor CsV_3Sb_5. *Nat. Phys.* **18**, 301–308 (2022).
148. Song, D. et al. Orbital ordering and fluctuations in a kagome superconductor CsV_3Sb_5. *Sci. China Phys. Mech. Astron.* **65**, 247462 (2022).
149. Tazai, R., Yamakawa, Y., Onari, S. & Kontani, H. Mechanism of exotic density-wave and beyond-Migdal unconventional superconductivity in kagome metal AV_3Sb_5 (A = K, Rb, Cs). *Sci. Adv.* **8**, abl4108 (2022).
150. Neupert, T. et al. Charge order and superconductivity in kagome materials. *Nat. Phys.* **18**, 137–143 (2022).
151. Kenney, E., Ortiz, B., Wang, C., Wilson, S. & Graf, M. Absence of local moments in the kagome metal KV_3Sb_5 as determined by muon spin spectroscopy. *J. Phys. Condens. Matter* **33**, 235801 (2021).
152. Yang, S.-Y. et al. Giant, unconventional anomalous Hall effect in the metallic frustrated magnet candidate, KV_3Sb_5. *Sci. Adv.* **6**, eabb6003 (2020).
153. Yu, F. H. et al. Concurrence of anomalous Hall effect and charge density wave in a superconducting topological kagome metal. *Phys. Rev. B* **104**, L041103 (2021).
154. Feng, X., Jiang, K., Wang, Z. & Hu, J. Chiral flux phase in the kagome superconductor AV_3Sb_5. *Sci. Bull.* **66**, 1384–1388 (2021).
155. Denner, M. M., Thomale, R. & Neupert, T. Analysis of charge order in the kagome metal AV_3Sb_5 (A = K, Rb, Cs). *Phys. Rev. Lett.* **127**, 217601 (2021).
156. Lin, Y.-P. & Nandkishore, R. M. Complex charge density waves at van Hove singularity on hexagonal lattices: Haldane-model phase diagram and potential realization in the kagome metals AV_3Sb_5 (A=K, Rb, Cs). *Phys. Rev. B* **104**, 045122 (2021).
157. Mielke, C. III. et al. Time-reversal symmetry-breaking charge order in a kagome superconductor. *Nature* **602**, 245–250 (2022).
Evidence for time-reversal-symmetry-breaking charge order via a magnetic-moment-sensitive probe.
158. Guguchia, Z. et al. Tunable nodal kagome superconductivity in charge ordered RV_3Sb_5. Preprint at https://arxiv.org/abs/2202.07713 (2022).
159. Khasanov, R. et al. Charge order breaks time-reversal symmetry in CsV_3Sb_5. *Phys. Rev. Res.* **4**, 023244 (2022).
160. Xu, Y. et al. Three-state nematicity and magneto-optical Kerr effect in the charge density waves in kagome superconductors. *Nat. Phys.* https://doi.org/10.1038/s41567-022-01805-7 (2022).
161. Guo, C. et al. Switchable chiral transport in charge-ordered CsV_3Sb_5. *Nature* **611**, 461–466 (2022).
162. Teng, X.-K. et al. Discovery of charge density wave in a correlated kagome lattice antiferromagnet. *Nature* **609**, 490–495 (2022).
163. Yin, J.-X. et al. Discovery of charge order and corresponding edge state in kagome magnet FeGe. *Phys. Rev. Lett.* **129**, 166401 (2022).
164. Mazin, I. I. et al. Theoretical prediction of a strongly correlated Dirac metal. *Nat. Commun.* **5**, 4261 (2014).
165. Yu, F. H. et al. Unusual competition of superconductivity and charge-density-wave state in a compressed topological kagome metal. *Nat. Commun.* **12**, 3645 (2021).
166. Chen, K. Y. et al. Double superconducting dome and triple enhancement of T_c in the kagome superconductor CsV_3Sb_5 under high pressure. *Phys. Rev. Lett.* **126**, 247001 (2021).
167. Du, F. et al. Pressure-induced double superconducting domes and charge instability in the kagome metal KV_3Sb_5. *Phys. Rev. B* **103**, L220504 (2021).
168. Song, Y. et al. Competition of superconductivity and charge density wave in selective oxidized CsV_3Sb_5 thin flakes. *Phys. Rev. Lett.* **127**, 237001 (2021).
169. Chen, X. et al. Highly robust reentrant superconductivity in CsV_3Sb_5 under pressure. *Chin. Phys. Lett.* **38**, 057402 (2021).
170. Zhu, C. C. et al. Double-dome superconductivity under pressure in the V-based kagome metals AV_3Sb_5 (A=Rb and K). *Phys. Rev. B* **105**, 094507 (2022).
171. Oey, Y. et al. Fermi level tuning and double-dome superconductivity in the kagome metals $CsV_3Sb_{5-x}Sn_x$. *Phys. Rev. Mater.* **6**, L041801 (2022).
172. Li, Y. et al. Tuning the competition between superconductivity and charge order in kagome superconductor $Cs(V_{1-x}Nb_x)_3Sb_5$. *Phys. Rev. B* **105**, L180507 (2022).
173. Emery, V. J. & Kivelson, S. A. Importance of phase fluctuations in superconductors with small superfluid density. *Nature* **374**, 434–437 (1995).
174. Mu, C. et al. S-wave superconductivity in kagome metal CsV_3Sb_5 revealed by $^{121/123}$Sb NQR and ^{51}V NMR measurements. *Chin. Phys. Lett.* **38**, 077402 (2021).
175. Gupta, R. et al. Microscopic evidence for anisotropic multigap superconductivity in the CsV_3Sb_5 kagome superconductor. *npj Quantum Mater.* **7**, 49 (2022).
176. Wu, X. et al. Nature of unconventional pairing in the kagome superconductors AV_3Sb_5 (A = K, Rb, Cs). *Phys. Rev. Lett.* **127**, 177001 (2021).
177. Xu, H.-S. et al. Multiband superconductivity with sign-preserving order parameter in kagome superconductor CsV_3Sb_5. *Phys. Rev. Lett.* **127**, 187004 (2021).
178. Duan, W. et al. Nodeless superconductivity in the kagome metal CsV_3Sb_5. *Sci. China Phys. Mech. Astron.* **64**, 107462 (2021).
179. Gu, Y. et al. Gapless excitations inside the fully gapped kagome superconductors AV_3Sb_5. *Phys. Rev. B* **105**, L100502 (2022).
180. Lou, R. et al. Charge-density-wave-induced peak–dip–hump structure and the multiband superconductivity in a kagome superconductor CsV_3Sb_5. *Phys. Rev. Lett.* **128**, 036402 (2022).
181. Keimer, B. & Moore, J. The physics of quantum materials. *Nat. Phys.* **13**, 1045–1055 (2017).
182. Gao, Z.-A. Design and synthesis of a single-layer ferromagnetic metal–organic framework with topological nontrivial gaps. *J. Phys. Chem. C* **124**, 27017–27023 (2020).
183. Fuchs, M. et al. Kagome metal–organic frameworks as a platform for strongly correlated electrons. *J. Phys. Mater.* **3**, 025001 (2020).
184. Asaba, T. et al. Colossal anomalous Nernst effect in a correlated noncentrosymmetric kagome ferromagnet. *Sci. Adv.* **7**, abf1467 (2021).
185. Chen, T. et al. Large anomalous Nernst effect and nodal plane in an iron-based kagome ferromagnet. *Sci. Adv.* **8**, abk1480 (2022).
186. Muechler, L. et al. Emerging chiral edge states from the confinement of a magnetic Weyl semimetal in $Co_3Sn_2S_2$. *Phys. Rev. B* **101**, 115106 (2020).
187. Howard, S. et al. Evidence for one-dimensional chiral edge states in a magnetic Weyl semimetal $Co_3Sn_2S_2$. *Nat. Commun.* **12**, 4269 (2021).

188. Regnault, N. et al. Catalogue of flat-band stoichiometric materials. *Nature* **603**, 824–828 (2022).
189. Rhim, J. W., Kim, K. & Yang, B. J. Quantum distance and anomalous Landau levels of flat bands. *Nature* **584**, 59–63 (2020).
190. Nayak, C., Simon, S. H., Stern, A., Freedman, M. & Sarma, S. D. Non-Abelian anyons and topological quantum computation. *Rev. Mod. Phys.* **80**, 1083 (2008).
191. Lian, B., Sun, X.-Q., Vaezi, A., Qi, X.-L. & Zhang, S.-C. Topological quantum computation based on chiral Majorana fermions. *Proc. Natl Acad. Sci. USA* **115**, 10938–10942 (2018).
192. Yan, S., Huse, D. A. & White, S. R. Spin-liquid ground state of the S=1/2 kagome Heisenberg antiferromagnet. *Science* **332**, 1173–1176 (2011).
193. He, Y.-C., Zaletel, M. P., Oshikawa, M. & Pollmann, F. Signatures of dirac cones in a DMRG study of the kagome Heisenberg model. *Phys. Rev. X* **7**, 031020 (2017).
194. Laughlin, R. B. Superconducting ground state of noninteracting particles obeying fractional statistics. *Phys. Rev. Lett.* **60**, 2677–2680 (1988).
195. Kalmeyer, V. & Laughlin, R. B. Theory of the spin liquid state of the Heisenberg antiferromagnet. *Phys. Rev. B* **39**, 11879–11899 (1989).
196. Kasahara, Y. et al. Majorana quantization and half-integer thermal quantum Hall effect in a Kitaev spin liquid. *Nature* **559**, 227–231 (2018).
197. Czajka, P. et al. Oscillations of the thermal conductivity in the spin-liquid state of α-$RuCl_3$. *Nat. Phys.* **17**, 915–919 (2021).
198. Di Sante, D. et al. Turbulent hydrodynamics in strongly correlated kagome metals. *Nat. Commun.* **11**, 3997 (2020).
199. Lima, F. C. Double flat bands in kagome twisted bilayers. *Phys. Rev. B* **100**, 155421 (2019).
200. Scheer, M. G., Gu, K. & Lian, B. Magic angles in twisted bilayer graphene near commensuration: towards a hypermagic regime. *Phys. Rev. B* **106**, 115418 (2022).

Acknowledgements We thank our research collaborators for various discussions on kagome physics. M.Z.H. acknowledges support from the US Department of Energy, Office of Science, National Quantum Information Science Research Centers, Quantum Science Center and Princeton University; visiting scientist support at Berkeley Lab (Lawrence Berkeley National Laboratory) during the early phases of this work; support from the Gordon and Betty Moore Foundation (GBMF9461) for the STM and the theory work; and support from the US DOE under the Basic Energy Sciences programme (grant number DOE/BES DE-FG-02-05ER46200) for the theory and angle-resolved photoemission spectroscopy work. B.L. is supported by the Alfred P. Sloan Foundation, the National Science Foundation through Princeton University's Materials Research Science and Engineering Center DMR-2011750; and the National Science Foundation under award DMR-2141966. J.-X.Y. acknowledges support from Princeton University, as well as the support from South University of Science and Technology of China principal research grant (number Y01202500). M.Z.H. also acknowledges visiting scientist support from Stanford University during the last phase of this work.

Author contributions All authors discussed the content of the manuscript, and reviewed and edited the entire manuscript.

Competing interests The authors declare no competing interests.

Additional information
Correspondence and requests for materials should be addressed to Jia-Xin Yin, Biao Lian or M. Zahid Hasan.
Peer review information *Nature* thanks Domenico Di Sante, Madhav Ghimire and the other, anonymous, reviewer(s) for their contribution to the peer review of this work.
Reprints and permissions information is available at http://www.nature.com/reprints.